Understanding the impact of halogenation on the crystalline photomechanical response properties of 9-anthracene carboxylic acid from first-principles

Cody J. Perry and Gregory J. O. Beran*

Department of Chemistry, University of California, Riverside, California 92521 USA

E-mail: gregory.beran@ucr.edu

Abstract

Photomechanical organic crystals transform light into mechanical work via solid-state photochemical reactions. While many examples of photomechanical systems have been demonstrated, significant gaps in understanding the relationships between the chemical structure of the photochrome molecule, its crystal structure, and the associated photomechanical response remain. Focusing on the case of [4+4] photodimerization of 9-anthracene carboxylic acid, this density-functional theory study examines that impact of replacing hydrogen atoms with fluorine or chlorine in various positions on the photomechanical response. The results demonstrate how the interplay of intramolecular deformations and intermolecular crystal packing interactions means that even simple chemical substitutions that preserve the overall crystal packing motif can impact the photochemical response in ways that are not obvious *a priori*. In addition, the changes in work density obtained from the halogenated species here are an order of magnitude smaller than what previous work found can be obtained through varying the

crystal packing motif. This suggests that crystal engineering should take precedence when trying to increase the work density of a system, while additional minor molecular modifications can be used to refine the photomechanical response further or to tune other properties of the material.

Introduction

Photomechanical crystals convert light into mechanical work via solid-state cycloadditions, cis-trans isomerizations, and ring-opening/closing reactions, and other photochemical reactions.[1–6] Organic crystals are characterized by a unique combination of high elastic modulus and potentially large structural deformations that means they can potentially achieve exceptional volumetric work densities up to ∼10–100 MJ/m^3.[6–9] As a result, photomechanical crystals can move objects that are several orders of magnitude heavier than themselves,[10–13] operate gear wheels,[14] and perform other useful mechanical functions.[6] In many systems, the photomechanical transformations are either thermally or photochemically reversible, which can be important for practical devices.

Anthracenes represent one promising class of photomechanical crystal which have been studied in considerable detail.[1,6,15,16] Solid-state [4+4] photodimerization reactions of anthracene derivatives and/or photomechanical responses have been demonstrated experimentally for many different species, including 9-methyl anthracene,[16–21] 9-carboxylate ester anthracenes,[22,23] 9-cyanoanthracene,[16,24,25] 9-anthraldehyde,[26,27] (*E*)-2-(9-anthrylmethylene)-1-indanone,[28] and 9-anthracene carboxylic acid (9AC).[16,29–31] The [4+4] photodimerization reaction (Figure 1a) exhibits negative photochromism, which can enable (near-)complete photochemical conversion of the crystal, even in optically thick crystals. Micro- and nanoscale crystals of anthracene derivatives can exhibit photomechanical elongation,[22] bending,[32] and twisting,[33] depending on the crystal morphology.

In 9AC, the solid-state photodimerization reaction rapidly and spontaneously reverts back to the monomer species, and it can be cycled repeatedly.[32] Various molecular derivatives of

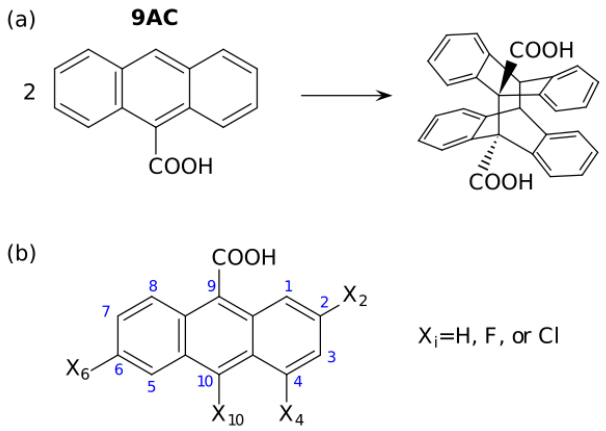

Figure 1: (a) The solid-state [4+4] photodimerization of 9AC reaction generates the product with a head-to-head arrangement of the carboxylic acid groups. (b) The 9AC derivatives considered here involve mono-halogenation with F or Cl at the 2, 4, or 10 positions, or dihalogenation at the 2 & 6 positions.

9AC have been synthesized in an effort to tune the material properties.[29–31] Many of these derivatives replace the hydrogens in the 2, 4, 5, 6, and/or 10 positions with fluorines or chlorines (Figure 1b). The resulting species often maintain the same crystal packing motif as 9AC but modify its elastic modulus, hardness, photodimer dissociation rate, and mechanical recovery. For example, substituting a fluorine at the 4 position of 9AC (4F-9AC) leads to a crystal that is less brittle, which reverts back to the monomer much more quickly, and which can be cycled an order of magnitude more times than 9AC itself.[30,31] Despite considerable experimental work, however, a clear understanding for how altering the molecular structure impacts the crystalline photomechanical response remains elusive. As a result, the search for new and improved photomechanical crystals has often been carried out in a time-consuming trial-and-error fashion.[6]

Computational chemistry predictions can help bridge between molecular structure and photomechanical response. For example, the combination of solid-state nuclear magnetic resonance (NMR) experiments, density-functional theory (DFT) modeling of candidate crystal structures, and NMR chemical shift predictions helped solve the crystal structure of the solid-state reacted dimer (SSRD) polymorph of 9-tert-butyl anthracene ester (9TBAE)[34] and established an atomistic mechanism for the photomechanical transformation.[35] Another

computational study investigated the energetic relationships between crystals of the 9TBAE monomer, its SSRD polymorph, and the solution-grown product polymorph formed by crystallizing the 9TBAE photodimer species from solution.[36] A DFT-driven crystal structure prediction study gave insight into the crystal packing tendencies that govern the solid-state photoreactivity of two cinnamalmalonitrile derivatives.[37] Finally, a series of primarily gas-phase DFT calculations showed a relationship between the predicted [4+4] photodimerization reaction energy and experimental reactivity for a series of halogenated 9AC derivatives.[31]

In many (but not all[16]) photomechanically active anthracene crystals, the anthracene molecules pack with a suitable co-facial angle and intermolecular distance[15] for the reactions occur topochemically. We have recently developed a computational framework for predicting the structural response generated by the topochemical photomechanical transformation of a molecular crystal and for characterizing the ideal work potentially produced by the photomechanical engine.[38] Starting from the crystal structure of the reactant, the structure of the solid-state reacted dimer (SSRD) is predicted computationally by replacing the reactant molecules in the lattice with their corresponding photochemical products and relaxing with DFT. By assuming a fast and complete transformation from reactant to product molecules in the crystal, the ideal work density that can be performed by the photomechanical transformation can be computed based on the stress created in the crystal lattice upon reacting the molecules and the strain relieved by the subsequent crystal deformation.

Previous work demonstrates that this topochemical approach correctly predicts the photomechanical transformations in crystals of 9-methyl anthracene,[38] 9-tert-butyl anthracene ester (9TBAE),[38] and in a diarylethene species.[39] Investigating the ideal work densities predicted for each of these photomechanical transformations has proved useful for relating between the structure of a molecule, its crystal packing, and the photomechanical response. For example, studying the predicted photomechanical responses of a series of diarylethene crystal polymorphs revealed how changes in crystal packing can alter the maximum ideal photomechanical work density for a given species by an order of magnitude.[39] The largest

work densities are achieved by packing the photochrome molecules so as to align the crystal deformation along a single crystallographic direction, thereby producing a highly anisotropic structural response.

While the importance of crystal packing has been demonstrated, it remains unclear how chemical modifications to the molecular photochrome impact the photomechanical response, especially in cases where the different chemical derivatives retain the same qualitative crystal packing motif. To elucidate the effects of such molecular modifications, the theoretical photomechanical responses for a series of halogenated 9AC derivatives are studied here. We find that the halogen substitutions considered here can increase or decrease the predicted ideal work densities for 9AC by a factor of two. Such variations in work density are considerably smaller than what can be achieved through control over crystal packing, but they may still be useful for refining the photomechanical response of a given material or for tuning its other mechanical characteristics, photophysical properties, and/or processing conditions.

In addition, the present study helps rationalize the often highly anisotropic work densities for these different derivatives in terms of the atomistic changes in the crystal structure. The direction of maximum work density in the crystals of these 9AC derivatives often aligns with the buckling of the anthracene rings, but sometimes it derives more from changes in the intermolecular spacing between photodimers. Such subtleties reiterate the difficulty of anticipating the relationships between molecular structure and the crystalline photomechanical response based on chemical intuition alone. On the other hand, the work here shows how first-principles computational modeling can bridge this gap, which could be useful for future efforts that seek to understand, improve, or even design the photomechanical response properties of a crystal.

Methods

Experimental structures for seven 9AC crystals were obtained from the Cambridge Crystal Structure Database (CSD). The crystals includes monoclinic 9AC (CSD reference code QQQFDJ01), triclinic 9AC (QQQFDJ02), and a series of derivatives which are denoted by the positions of the halogen substitutions, as indicated in Figure 1b: 2F-9AC (YOYCAS), 4F-9AC (YOYCEW), 10F-9AC (PAMCAJ), 2,6diF-9AC (YOYCIA), and 10Cl-9AC (PAMCEN). Several of these experimental crystal structures exhibit disorder in the orientations of the halogen atoms. In those cases, a single disorder component was selected.

To complete the set of derivatives and investigate the role of the halogen atom type, additional hypothetical 2Cl-9AC, 4Cl-9AC, and 2,6diCl-9AC chlorine analogs were created by replacing fluorines with chlorines without changing the qualitative crystal packing motif. Organic crystal packing can be sensitive to small changes in the molecular structure, and these hypothetical chlorine analogs derived from the crystal structure of the fluorinated species may or may not correspond to the true crystal structures one would obtain experimentally. Regardless, they provide a useful, controlled theoretical comparison for how small changes in molecular structure impact the photomechanical response properties when the same general crystal packing motif is retained. All experimental and hypothetical crystal structures were fully optimized with dispersion-corrected DFT under periodic boundary conditions, relaxing both the lattice vectors and the atomic positions (variable-cell optimization). Further details of the electronic structure calculations will be described below.

Modeling the photomechanical engines

The theoretical photomechanical engine cycle[38] used to model the photomechanical transformation and compute the ideal work density is shown in Figure 2. This thermodynamic cycle begins with the crystal structure of the reactant. Step 1 involves the complete and instantaneous conversion of all reactant monomers to the product dimers with no change

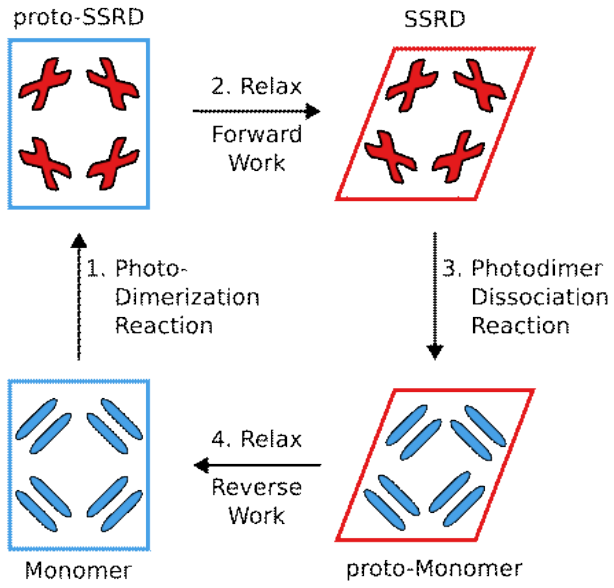

Figure 2: Schematic of the ideal ideal photomechanical engine cycle[38] used to compute the photomechanical work density that can be performed by a given species and crystal structure. The engine cycle alternates between fast, complete photodimerization or dissociation reactions within a fixed unit cell (Steps 1 & 3) and subsequent relaxation of the lattice parameters to deform the crystal and perform work (Steps 2 & 4).

in the crystal lattice parameters, producing the proto-SSRD. Assuming fast and complete reaction should maximize the stress created within the unit cell, and it therefore gives an upper limit to the potential work that can be produced upon subsequent relaxation of the lattice. Step 2 relaxes the proto-SSRD crystal to the equilibrium SSRD structure. This relaxation produces work in the "forward" stroke direction by relieving the stress and strain inherent to the proto-SSRD. In Step 3, a complete and instantaneous thermal dissociation of the photodimer regenerates the original monomer molecules within the SSRD unit cell (proto-monomer). Step 4 relaxes the proto-monomer back to the equilibrium monomer crystal structure, thereby producing work in the "reverse" stroke direction.

Previous work has identified how the thermodynamic asymmetry in the reactant and product potential energy surfaces typically means that less work is produced by the reverse stroke (Step 4) than the forward one (Step 2).[39] For this reason, the present paper focuses primarily on understanding how halogenating 9AC impacts the forward direction portion (Steps 1 and 2) of the photomechanical engine cycle. The structures, energetics, and work

densities for the reverse directions (Steps 3 and 4) have been computed only for several representative systems here: monoclinic and triclinic 9AC, 4F-9AC, 2,6-diF-9AC, 10F-9AC, and 10Cl-9AC, the results of which can be found in the Supporting Information (SI).

To generate the proto-SSRD crystal structure, the molecules in the reactant crystal were reacted topochemically as described in ref 38. Specifically, the reactant monomers in the unit cell are replaced with the product dimers, positioned at the same centers of mass and oriented to minimize atomic displacements. A supercell representation of the reactant crystal was used to include the reacting pairs as needed. Because 9AC crystals exhibit one-dimensional stacks of anthracenes with hydrogen bonding between them, the experimental photodimerization reactions occur stochastically within the stacks, and 100% conversion is not achieved.[33,40] For the idealized periodic DFT calculations involving small periodic unit cells here, however, 100% conversion is assumed. Pairs of photodimerization reactions were performed within tetramer sub-clusters in the crystal. As shown in Figure 3a, the tetramer unit involves two π-stacked anthracenes with head-to-head carboxylic acid groups that are hydrogen bonded to an adjacent pair of π-stack of anthracenes. This is consistent with how the gas-phase tetramers were modeled in ref 31.

After reacting the monomers topochemically, the final proto-SSRD crystal structure is obtained by relaxing the atomic positions of the photodimer molecules within the fixed lattice constants of the reactant monomer crystal. Next, an unconstrained variable-cell optimization is performed on the proto-SSRD to relax it to the equilibrium SSRD structure. From the DFT stress tensor (σ) for the proto-SSRD and the strain tensor (ϵ) derived from the lattice parameter changes between the proto-SSRD and relaxed SSRD structures, the elastic work density is calculated according to

$$W(\hat{n}) = -\frac{1}{2}\hat{n}^{\intercal}\sigma\epsilon\hat{n} \tag{1}$$

Because the structural transformation is anisotropic, the work is computed as a function of

the crystallographic direction, specified by the unit vector $\hat{n}$. After sampling over all possible spherical polar angles, the resulting work density is plotted as a heat map on the surface of a sphere. See ref 39 for further details and the complete set of mathematical expressions required to perform these calculations. DFT lattice parameters and stress tensors for all crystals studied here are provided in SI Section S3. for the sake of reproducibility. The same methodology is applied to study the reverse-direction dissociation reaction (Steps 3 and 4 in Figure 2), constructing the proto-monomer structure by replacing the product dimers with a pair of reactant monomers and performing the corresponding fixed-cell and variable-cell geometry optimizations.

Electronic structure calculations

All crystal structures were optimized in Quantum Espresso v6.5[41] using planewave DFT with the B86bPBE functional[42,43] and exchange hole dipole moment (XDM) dispersion correction[44] under periodic boundary conditions. A 50 Ry planewave cutoff was utilized with a Monkhort-Pack reciprocal space k-point grid density of at least 0.05 $Å^{-1}$. The projector augmented wave (PAW) pseudo-potential was implemented in Quantum Espresso for the core electrons.

Approximate density functionals, especially generalized gradient approximation (GGA) functionals such as the one used here, suffer from density-driven delocalization error.[45,46] The functionals artificially stabilize species with more delocalized densities relative to those with more localized electronic structure. In the context of anthracene photodimerization, the GGA functionals used for the crystal calculations artificially destabilize the photodimer product by up to ∼50–70 kJ/mol relative to the monomer reactants.[36,38,47,48]

To address the delocalization error here, an intramolecular correction[49] is applied which replaces the DFT intramolecular energies of the monomer and photodimer with the energies computed using a correlated wavefunction method that does not suffer from delocalization error. Specifically, the corrected single-point energies are calculated by taking the DFT

energy of the crystal, subtracting out the DFT monomer energies and adding the dispersion-corrected spin-component-scaled MP2[48] energies.

$$E_{corrected} = E_{crystal}^{DFT} + \sum_i \left(E_{molec,i}^{SCS-MP2D} - E_{molec,i}^{DFT} \right) \quad (2)$$

Due to crystal symmetry in 9AC and its derivatives, the molecular calculations only need to be performed for a single monomer of photodimer, and the results can be multiplied by the number of molecules in the unit cell.

The molecular DFT energies were calculated using QuantumEspresso (with the same settings as for the crystals) and a large orthorhombic unit cell which mimics the gas phase by reducing the intermolecular interactions between periodic images. The dimensions of the unit cell were defined as $(L_x + 20\ \text{Å}) \times (L_y + 20\ \text{Å}) \times (L_z + 20\ \text{Å})$, with L_n being the length of the molecule in each Cartesian direction x, y, and z. The SCS-MP2D calculations were performed using Psi4 v1.5[50] and the MP2D library.[51] The MP2 correlation energies were extrapolated to the complete-basis-set limit using two-point extrapolation[52] from the aug-cc-pVTZ and aug-cc-pVQZ basis sets,[53] and they were combined with Hartree-Fock/aug-cc-pVQZ energies.

This intramolecular correction approach has been successfully demonstrated for anthracenes,[36,38,48] pharmaceuticals,[49,54] organic semiconductor materials,[55] and other organic crystals.[49,56,57] For the 9AC derivatives studied here, the median and maximum single-point energy corrections to the DFT energies are a substantial 62 and 74 kJ/mol, respectively (SI Table S2), highlighting the importance of the correction.

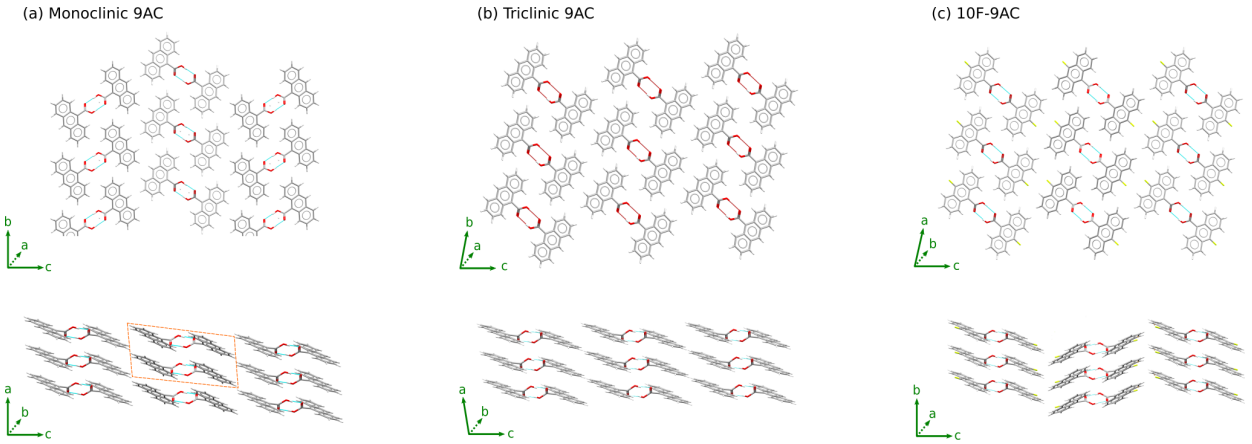

Figure 3: Comparison of the crystal packing motifs of (a) monoclinic 9AC, (b) triclinic 9AC, and (c) 10F-9AC along two different crystallographic axes. The other 9AC derivatives studied here adopt the same packing as monoclinic 9AC. The photodimerization reactions are modeled to occur within tetramer sub-clusters, such as the one exemplified by the orange box in (a). All molecules in the crystal are reacted to simulate 100% conversion.

Results and Discussion

Crystal structures of the 9AC derivatives

Most of the crystal structures studied here adopt the same qualitative crystal packing as monoclinic 9AC, which is shown in Figure 3a. It involves hydrogen-bonded carboxylic acid dimers arranged in one-dimensional stacks along the a axis, and these stacks align along the b axis. These aligned stacks repeat along the c direction, rotating by 90° between each row. However, two of the crystal structures considered adopt slightly different packing motifs. Triclinic 9AC[33] differs from monoclinic 9AC in the orientations of these aligned stacks along the c direction (Figure 3b). The anthracene stacks in the triclinic polymorph are also shifted slightly relative to one another along a to create planar sheets. For 10F-9AC (Figure 3c), the crystal packing seen when looking down the b axis is similar to that seen along the a axis of triclinic 9AC, but the relative angles between adjacent stacks along c differ. Despite these packing differences, all the crystals examined here have the molecules suitably aligned for [4+4] photodimerization reactions to occur within the π-stacked anthracenes (e.g. along

Table 1: DFT-predicted percent changes in the crystal lattice parameters a, b, c, α, β, γ and unit cell volume V upon solid-state [4+4] photodimerization of the various 9AC derivatives. The maximum ideal anisotropic work density for the forward-direction photodimerization reaction is also listed.

Species	Δa (%)	Δb (%)	Δc (%)	$\Delta\alpha$ (%)	$\Delta\beta$ (%)	$\Delta\gamma$ (%)	ΔV (%)	Max. Work Density (MJ/m^3)
Monoclinic 9AC	+1.1	+3.8	+3.0	-	-7.3	-	+6.1	30
Triclinic 9AC	+2.0	+2.2	+2.5	-0.9	+4.3	-3.4	+6.1	35
2F-9AC	-1.3	+3.7	+2.4	-	-1.9	-	+8.0	23
2Cl-9AC[a]	+1.0	+3.1	+2.4	-	-1.1	-	+6.7	15
4F-9AC	+0.8	+2.0	+5.5	-	-7.2	-	+7.9	52
4Cl-9AC[a]	+0.7	+1.9	+5.4	-	-5.9	-	+8.2	59
2,6diF-9AC	+0.6	+2.6	+1.5	-	-0.9	-	+4.8	14
2,6diCl-9AC[a]	-0.1	+7.0	-0.5	-	-0.7	-	+6.4	70
10F-9AC	+2.9	+0.9	+0.7	+0.1	+2.8	+0.1	+6.3	30
10Cl-9AC[b]	-0.8	-0.4	+4.4	-	-5.0	-	+3.7	40

[a] Hypothetical crystal structure.

[b] Solid-state photodimerization does not occur experimentally.

the a axis in monoclinic 9AC) without significantly disrupting the hydrogen bonding.

The DFT-optimized crystal structures retain very good agreement with experiment, with 15-molecule root-mean-square-deviations (rmsd15)[58] values less than 0.2 Å (SI Table S3). Examination of the optimized crystal structures indicates that fluorination increases the molar volume by ∼3–5% compared to monoclinic 9AC, with the di-fluorinated crystals being larger than the mono-fluorinated ones. The chlorinated crystal volumes are up to 10% larger than 9AC. These volume changes are unsurprising, but they point to modest changes in the intermolecular forces between monomer stacks.

9AC crystals undergo the solid-state [4+4] photodimerization reaction shown in Figure 1a. The formation of new carbon-carbon bonds and change in hybridization from sp^2 to sp^3 at carbons 9 and 10 buckles the aromatic rings outward. To understand the impact of this reaction on 9AC crystal structures, we apply the photomechanical engine cycle as described in the Methods section. Pairs of 9AC monomers are reacted topochemically and the structures of the proto-SSRD and equilibrium SSRD are determined via DFT optimization. The anisotropic ideal work densities associated with the crystal deformations are computed from the associated stress and strain tensors. Table 1 summarizes the predicted changes in

lattice parameters for the different crystals due to the photochemical reaction, the change in unit cell volume, and the maximum the work density found across all crystallographic directions for each crystal. Figure 4 shows several representative crystal structure overlays that indicate how the structures change after the photochemical reaction. Figure 5 plots the anisotropic work densities for several representative crystals as a heat map on a sphere, highlighting the crystallographic directions in which the largest amount of work is performed. Analogous overlays and work density plots for the other crystals can be found in SI Sections S2 and S3. The following sections examine the behaviors for the different 9AC derivatives in detail.

Photomechanical response in 9AC

Consider first monoclinic and triclinic 9AC. The photomechanical response of monoclinic 9AC was already modeled using the same techniques in ref 38; those results are repeated here for convenience. The buckling of the anthracene rings after photodimerization pushes the molecules apart, leading to a 7.3% decrease in the β angle and smaller percentage increases along the a, b, and c axes. Due to the large change in the β angle, the maximum predicted work of 30 MJ/m^3 occurs in a direction in between the a and c axes (Figure 5a). For context, ref 38 predicted maximum ideal work densities of 25 MJ/m^3 for 9-methyl anthracene, and 47 MJ/m^3 for 9TBAE, while the maximum work densities obtained for different polymorphs of two diarylethenes ranged from 5–200 MJ/m^3.[39]

Although the specific lattice parameter changes for triclinic 9AC differ from the monoclinic form, its maximum predicted work density of 35 MJ/m^3 is very similar to the monoclinic polymorph. This contrasts the twenty-fold difference in the maximum work densities predicted for two different crystal packing motifs of a diarylethene.[39] The key to this discrepancy lies in the similarity in the crystal packing: the two diarylethene structures exhibit completely different packing motifs, and they have very different maximim work densities. On the other hand, monoclinic and triclinic 9AC exhibit very similar crystal packing (Fig-

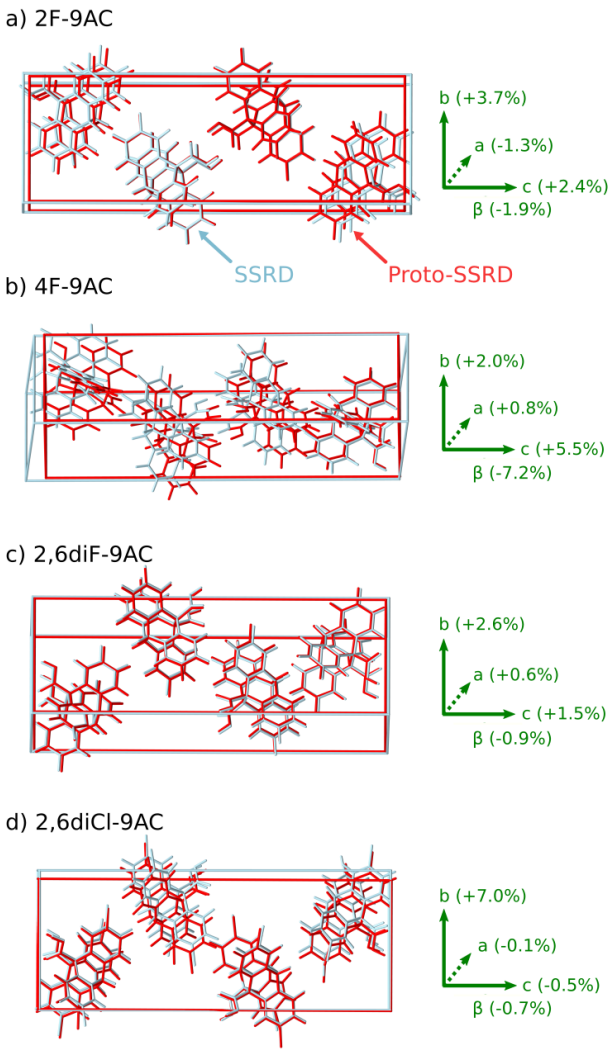

Figure 4: Crystal structure overlays comparing the proto- and equilibrium SSRD structures for (a) 2F-9AC, (b) 4F-9AC, (c) 2,6diF-9AC, and (d) 2,6diCL-9AC. The percent changes in the lattice parameters from Monomer/proto-SSRD to equilibrium SSRD are indicated.

ure 3a,b) and similar work densities. The nominal crystallographic direction in which the maximum 9AC work occurs differs between the two polymorphs (Figure 5a,b) due to the different representations of the two 9AC unit cells, but it generally aligns with the direction of the anthracene ring buckling in both cases. For comparison, the maximum work density in 9TBAE also aligns with the anthracene buckling direction.[38]

In the experimental literature, there are conflicting reports about whether triclinic 9AC undergoes solid-state photodimerization. Zhu et al report a rapid, reversible solid-state re-

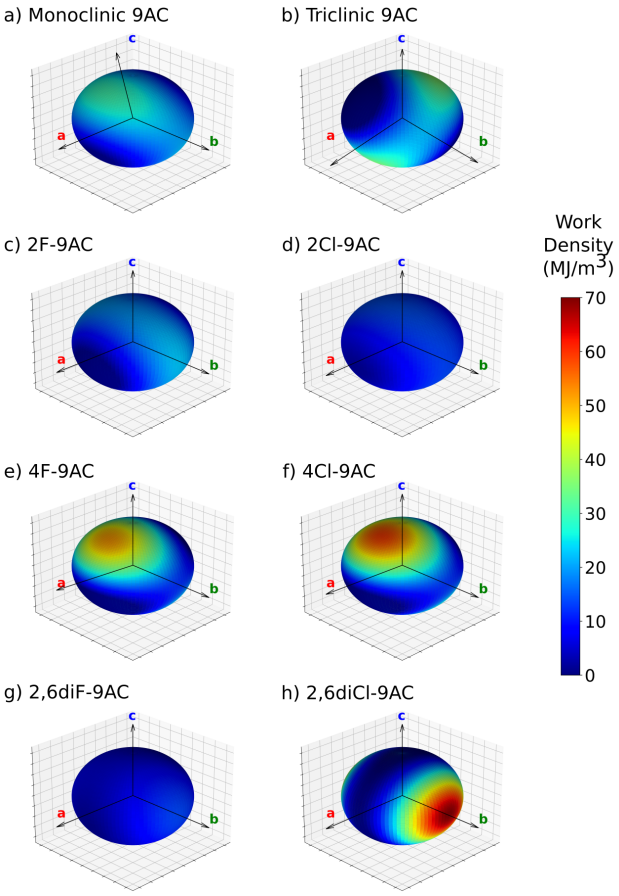

Figure 5: Predicted anisotropic work density heat maps (in MJ/m^3) for solid-state photodimerization reactions of 9AC and selected derivatives. The crystallographic axes are indicated in each plot. More highly ansiotropic crystal transformations generally produce larger maximum work densities, with 2,6diCl-9AC exhibiting the largest work density here of 70 MJ/m^3 along the *b* crystallographic axis.

action.[29] On the other hand, Salzillo and Brillante observed no changes in the lattice phonon spectrum upon irradiation, though they did observe an uncharacterized morphological change in the crystals.[16] They suggest that the triclinic crystals are either non-reactive or that the reverse photodimer dissociation reaction occurs very quickly.

Figure 6 shows the energy changes associated with each step of the photomechanical engine cycle for both monoclinic and triclinic 9AC. The photodimerization reaction energetics are very similar for both polymorphs, with the photodimerization reaction of the triclinic form actually being about 6 kJ/mol less endothermic than the monoclinic polymorph. In other words, there does not appear to be any thermodynamic reason why the triclinic form

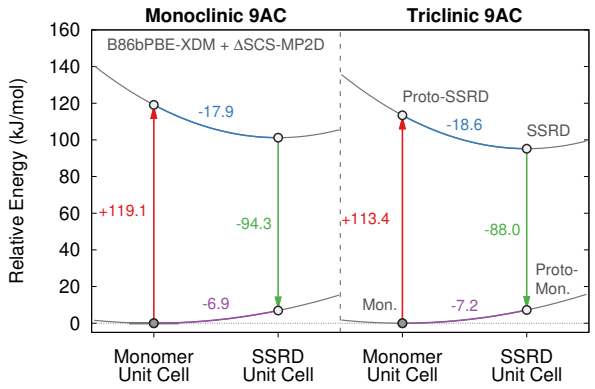

Figure 6: Photomechanical engine cycle energies for the two polymorphs of 9AC (in kJ/mol). The lower curve schematically represents the monomer reactant crystal potential energy surface (PES), while the upper curve corresponds to the product photodimer PES.

should not undergo a solid-state reaction. A detailed investigation of the photochemical kinetics of the solid-state transformation would provide further insights into the reactivity of these two forms, but that is beyond the scope of the present study.

Effects of fluorine substitutions

To investigate how small chemical modifications to the photochrome impact the photomechanical response, we apply the same photomechanical engine modeling approach to the fluorinated 9AC derivatives: 2F-9AC, 4F-9AC, 10F-9AC, and 2,6,diF-9AC. The results in Table 1 demonstrate how the photomechanical response varies with the position of the fluorine group(s). For example, the 8.0% volume increase of 2F-9AC upon photodimerization is larger than the 6.1% one in monoclinic 9AC, yet the maximum work density produced by 2F-9AC of 23 MJ/m^3 is ∼25% smaller. The fluorine in the 2 position strengthens the interactions between neighboring dimer pairs and reduces the contraction of the β angle to 1.9%, versus 7.9% in monoclinic 9AC. The net result is that 2F-9AC deforms more isotropically overall (Figure 4a), leading to a lower maximum work density. 2,6diF-9AC similarly exhibits a relatively isotropic deformation, resulting in a maximum work density of only 14 MJ/m^3 (half that of monoclinic 9AC).

In contrast to those two fluorine derivatives, 4F-9AC has a maximum predicted work

density of 52 MJ/m^3, which is ∼70% larger than monoclinic 9AC. The 7.9% net volume increase in 4F-9AC is similar to that of 2F-9AC, but 4F-9AC produces a much larger maximum work density. Unlike the relatively isotropic changes in the aforementioned fluorinated species, 4F-9AC elongates 5.5% along c and shrinks the β angle by 7.2% (Figure 4b), making its transformation even more anisotropic than monoclinic 9AC. This larger deformation in 4F-9AC occurs along the primary expansion axis, leading to its larger maximum work density (Figure 5a,e). This differs from 2F-9AC, where the largest lattice deformation ends up being perpendicular to the buckling anthracene rings (Figure 4a), leading to a more isotropic distribution of the work density (Figure 5c). All of these results reinforce the importance of creating anisotropic structural changes to achieve the largest work densities.

10F-9AC is an outlier among these fluorine systems due to its different crystal packing motif. Nevertheless, it exhibits a similar ∼6% volume expansion to monoclinic 9AC and a similar maximum work density of 30 MJ/m^3. Interestingly, the fact that the anthracene rings exhibit two distinct orientations in 10F-9AC (Figure 3c) means that maximum work density does not clearly align with the anthracene ring buckling. In the end, the largest fractional lattice parameter change occurs along the a axis, and the maximum work is most closely aligned in that direction.

The reaction energies associated with the solid-state reactions in the fluorinated derivatives are only 5–10 kJ/mol larger than those in monoclinic 9AC (Figure 7). Moreover, the energies for the different steps of the engine cycle are also mostly similar across 9AC and most of its fluorinated derivatives (SI Table S1). The net photodimerization energy of 10F-9AC is somewhat larger than the others (Figure 7), due to both a large Step 1 energy and a smaller Step 2 relaxation energy. This reflects both the differences in crystal packing and the unfavorable steric clash between the two fluorine atoms in the 10 positions of each anthracene after photodimerization.

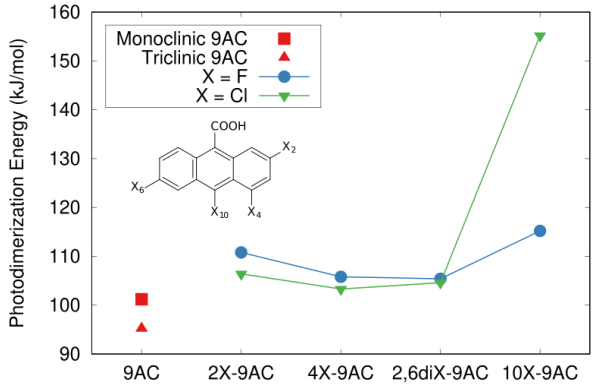

Figure 7: Summary of the net photodimerization energies, ΔE (2 Monomer $\rightarrow$ SSRD), for the 9AC and its derivatives (kJ/mol).

Effects of chlorine substitutions

Next we consider the chlorinated analogs of the fluorine derivatives to understand how changing the halogen impacts the photomechanical response. Because experimental crystal structures of 2Cl-9AC, 4Cl-9AC, and 2,6diCl-9AC have not been reported experimentally, hypothetical structure analogs were created by replacing the fluorines in 2F-9AC, 4F-9AC, and 2,6diF-9AC with chlorines. Modeling the photomechanical reaction of 2Cl-9AC produces results that are similar to 2F-9AC. Its 6.7% volume increase is modestly larger than for than monoclinic 9AC, but its maximum work density of 15 MJ/m^3 is only half that of 9AC. 4Cl-9AC also behaves similarly to 4F-9AC. The 4Cl-9AC volume change is slightly larger, and it generates a maximum work density of 59 MJ/m^3, which is about double that of monoclinic 9AC. As can be seen from Figure 5c–f, replacing fluorine with chlorine at either the 2 or 4 positions does not substantially impact the magnitude or directionality of the work density.

In contrast, the photomechanical response of 2,6diCl-9AC differs considerably from 2,6diF-9AC. Upon photodimerization, 2,6diCl-9AC expands 7% along the b direction (with minor changes in other directions), while 2,6diF-9AC transforms much more isotropically. In monoclinic 9AC or the 4-substituted 9ACs, the maximum work density aligns with the direction of anthracene buckling. However, in 2,6diCl-9AC, the buckling pushes the large chlorine atoms on adjacent molecules too close together, driving expansion along b to separate them

(Figure 4d). This leads to the large maximum work density of 70 MJ/m^3 along b, as shown in Figure 5h, which is orthogonal to the buckling direction. That steric clash is less pronounced for the smaller fluorine atoms in 2,6diF-9AC, leading to the smaller changes along b (Figure 4c) and smaller work densities seen in Figure 5g. In 9-methyl anthracene, which adopts a different crystal packing from 9AC, the direction of maximum work is also orthogonal to the anthracene buckling for similar steric reasons.[38]

Finally, consider 10Cl-9AC. Its crystal structure has been reported experimentally, and it resembles monoclinic 9AC rather than 10F-9AC. 10Cl-9AC actually does not photodimerize in the solid-state experimentally, despite having appropriately aligned anthracene monomers in the crystal. If it did react, the calculations suggest it would exhibit anisotropic expansion along the β angle and the c axis, similar to monoclinic 9AC. Its net volume change would be ∼40% smaller than for monoclinic 9AC, but because the deformation would be even more anisotropic, the maximum work of 40 MJ/m^3 would be ∼30% larger.

To understand why 10Cl-9AC does not react, consider the reaction energetics in Figure 7. The 155 kJ/mol photodimerization energy of 10Cl-9AC is at least 35 kJ/mol more endothermic than any of the other species studied here. This unfavorable reaction energy stems from the steric clash of having large chlorine atoms in the 10 position on each anthracene in the photodimer. In our earlier study that examined a number of 9AC derivatives in the gas-phase, we found that photodimerization reaction energies which exceed ∼90 kJ/mol (including 10Cl-9AC) were observed not to occur experimentally in the solid-state.[31] The calculations in the present study appear to be consistent with that general finding. The key difference here is that including the effects of the crystal lattice makes all of the reactions ∼35–45 kJ/mol more endothermic compared to the gas-phase. This implies that a better estimate of the thermodynamic energy threshold for solid-state photochemical reactivity of 9AC derivatives likely lies in the ∼125–135 kJ/mol range. Aside from 10Cl-9AC, the solid-state reaction energies for the chlorine derivatives are only a few kJ/mol less endothermic than for the fluorine derivatives (Figure 7).

Conclusions

Chemically modifying a successful molecular photochrome is a common strategy for trying to tune its photomechanical response properties. However, the lack of clear understanding for how changes in molecular structure will alter its solid-state behaviors often makes this a laborious trial-and-error process experimentally. The first-principles quantum chemistry approach used here bridges this gap and establishes an atomistic understanding for the photomechanical response of a given crystal structure. We have used this approach to examine how replacing hydrogen atoms with fluorine or chlorine impacts the photomechanical response of 9AC crystals. When the same crystal packing motif is maintained, we find that the maximum work densities of 9AC increase or decrease by roughly a factor of two across the derivatives studied here.

More important than the specific predicted work density values are the chemical insights relating to the design of photomechanical crystals. If the goal is to develop a photomechanical actuator device, knowledge of which crystallographic directions produce the most work is useful. The calculations show that the buckling of the anthracene rings is a major driver of stress in the crystal that often produces a large amount of work, but other factors can also play a role. For example, in 2,6diCl-9AC, the largest work density comes from steric clashes that push the molecules further apart in other crystallographic directions, while the non-parallel orientations of the anthracenes in the 10F-9AC crystal also impact the direction of maximum work. Such insights are not always obvious *a priori*, and the computational modeling is useful for understanding the photomechanical behaviors of specific crystals.

More generally, comparing the results here with those from our recent work on diarylethenes[39] reiterates the importance of crystal packing in determining work density. The variations in the maximum predicted work densities stemming from changes in crystal packing are up to an order of magnitude larger than the variations found here for the different halogenated derivatives. This suggests that efforts to maximize the work performance of an actuator should focus on engineering crystal packing motifs which produce highly anisotropic

photomechanical structure changes. Once the desired crystal packing has been achieved, smaller chemical changes to the molecular photochrome may be useful for tuning secondary properties of the material, such as its photophysics, stability for repeatable cycling, and/or processing suitability.

Acknowledgments

Support for this research from the National Science Foundation (CHE-1955554) and supercomputer time from ACCESS (CHE110064) to G.J.O.B. are gratefully acknowledged.

Conflict of Interest

The authors declare no conflicts of interest.

Supporting Information

- Tabulated solid-state reaction energetics, lattice parameters, stress tensors, as well as additional structure overlays and work density results (PDF).
- Crystallographic Information Files for all crystal structures modeled (CIF).

The Supporting Information is available free of charge at....

References

(1) Kim, T.; Zhu, L.; Al-Kaysi, R. O.; Bardeen, C. J. Organic Photomechanical Materials. *ChemPhysChem* **2014**, *15*, 400–414.

(2) Naumov, P.; Chizhik, S.; Panda, M. K.; Nath, N. K.; Boldyreva, E. Mechanically Responsive Molecular Crystals. *Chem. Rev.* **2015**, *115*, 12440–12490.

(3) Yu, Q.; Aguila, B.; Gao, J.; Xu, P.; Chen, Q.; Yan, J.; Xing, D.; Chen, Y.; Cheng, P.; Zhang, Z.; Ma, S. Photomechanical Organic Crystals as Smart Materials for Advanced Applications. *Chem. Eur. J.* **2019**, *25*, 5611–5622.

(4) Naumov, P.; Karothu, D. P.; Ahmed, E.; Catalano, L.; Commins, P.; Mahmoud Halabi, J.; Al-Handawi, M. B.; Li, L. The Rise of the Dynamic Crystals. *J. Am. Chem. Soc.* **2020**, *142*, 13256–13272.

(5) Huang, C.; Huang, R.; Zhang, S.; Sun, H.; Wang, H.; Du, B.; Xiao, Y.; Yu, T.; Huang, W. Recent Development of Photodeformable Crystals: From Materials to Mechanisms. *Research* **2021**, *2021*, 9816535.

(6) Awad, W. M. et al. Mechanical properties and peculiarities of molecular crystals. *Chem. Soc. Rev.* **2023**, *52*, 3098–3169.

(7) Mahmoud Halabi, J.; Ahmed, E.; Sofela, S.; Naumov, P. Performance of molecular crystals in conversion of light to mechanical work. *Proc. Nat. Acad. Sci.* **2021**, *118*, 1–7.

(8) Karothu, D. P.; Mahmoud Halabi, J.; Ahmed, E.; Ferreira, R.; Spackman, P. R.; Spackman, M. A.; Naumov, P. Global Analysis of the Mechanical Properties of Organic Crystals. *Angew. Chem. Int. Ed.* **2022**, *61*, e202113988.

(9) Karothu, D. P.; Ferreira, R.; Dushaq, G.; Ahmed, E.; Catalano, L.; Halabi, J. M.; Alhaddad, Z.; Tahir, I.; Li, L.; Mohamed, S.; Rasras, M.; Naumov, P. Exceptionally high work density of a ferroelectric dynamic organic crystal around room temperature. *Nat. Comm.* **2022**, *13*, 2823.

(10) Kobatake, S.; Takami, S.; Muto, H.; Ishikawa, T.; Irie, M. Rapid and reversible shape changes of molecular crystals on photoirradiation. *Nature* **2007**, *446*, 778–781.

(11) Morimoto, M.; Irie, M. A Diarylethene Cocrystal that Converts Light into Mechanical Work. *J. Am. Chem. Soc.* **2010**, *132*, 14172–14178.

(12) Dong, X.; Tong, F.; Hanson, K. M.; Al-Kaysi, R. O.; Kitagawa, D.; Kobatake, S.; Bardeen, C. J. Hybrid Organic–Inorganic Photon-Powered Actuators Based on Aligned Diarylethene Nanocrystals. *Chem. Mater.* **2019**, *31*, 1016–1022.

(13) Tong, F.; Xu, W.; Guo, T.; Lui, B. F.; Hayward, R. C.; Palffy-Muhoray, P.; Al-Kaysi, R. O.; Bardeen, C. J. Photomechanical molecular crystals and nanowire assemblies based on the [2+2] photodimerization of a phenylbutadiene derivative. *J. Mater. Chem. C* **2020**, *8*, 5036–5044.

(14) Terao, F.; Morimoto, M.; Irie, M. Light-Driven Molecular-Crystal Actuators: Rapid and Reversible Bending of Rodlike Mixed Crystals of Diarylethene Derivatives. *Angew. Chem. Int. Ed.* **2012**, *51*, 901–904.

(15) Schmidt, G. M. J. Photodimerization in the solid state. *Pure and Applied Chemistry* **1971**, *27*, 647–678.

(16) Salzillo, T.; Brillante, A. Commenting on the photoreactions of anthracene derivatives in the solid state. *CrystEngComm* **2019**, *21*, 3127–3136.

(17) Turowska-Tyrk, I.; Trzop, E. Monitoring structural transformations in crystals. 6. The [4 + 4] photodimerization of 9-methyl-anthracene. *Acta Cryst. B* **2003**, *59*, 779–786.

(18) Mabied, A. F.; Müller, M.; Dinnebier, R. E.; Nozawa, S.; Hoshino, M.; Tomita, A.; Sato, T.; Adachi, S. I. A time-resolved powder diffraction study of in-situ photodimerization kinetics of 9-methylanthracene using a CCD area detector and parametric Rietveld refinement. *Acta Cryst. B* **2012**, *68*, 424–430.

(19) Bąkowicz, J.; Turowska-Tyrk, I. The role of free space in photochemical reactions in

crystals at high pressure – the case of 9-methylanthracene. *Acta Cryst. B* **2022**, *78*, 223–230.

(20) Kim, T.; Zhu, L.; Mueller, L. J.; Bardeen, C. J. Mechanism of photoinduced bending and twisting in crystalline microneedles and microribbons composed of 9-methylanthracene. *J. Am. Chem. Soc.* **2014**, *136*, 6617–6625.

(21) Morimoto, K.; Kitagawa, D.; Tong, F.; Chalek, K.; Mueller, L. J.; Bardeen, C. J.; Kobatake, S. Correlating Reaction Dynamics and Size Change during the Photomechanical Transformation of 9-Methylanthracene Single Crystals. *Angew. Chem. Int. Ed.* **2022**, *61*, e202114089.

(22) Al-Kaysi, R. O.; Müller, A. M.; Bardeen, C. J. Photochemically Driven Shape Changes of Crystalline Organic Nanorods. *J. Am. Chem. Soc.* **2006**, *128*, 15938–15939.

(23) Zhu, L.; Agarwal, A.; Lai, J.; Al-Kaysi, R. O.; Tham, F. S.; Ghaddar, T.; Mueller, L.; Bardeen, C. J. Solid-state photochemical and photomechanical properties of molecular crystal nanorods composed of anthracene ester derivatives. *J. Mater. Chem.* **2011**, *21*, 6258–6268.

(24) Stevens, B.; Dickinson, T.; Sharpe, R. R. Photodimerization in Crystalline 9-Cyanoanthracene. *Nature* **1964**, *204*, 876–877.

(25) Cohen, M. D.; Ludmer, Z.; Thomas, J. M.; Williams, J. O. The role of structural imperfections in the photodimerization of 9-cyanoanthracene. *Proc. Roy. Soc. A* **1971**, *324*, 459–468.

(26) Al-Kaysi, R. O.; Zhu, L.; Al-Haidar, M.; Al-Muhannah, M. K.; El-Boubbou, K.; Hamdan, T. M.; Bardeen, C. J. Chemical reaction method for growing photomechanical organic microcrystals. *CrystEngComm* **2015**, *17*, 8835–8842.

(27) Chen, K.; Wang, J.; Feng, Y.; Liu, H.; Zhang, X.; Hao, Y.; Wang, T.; Huang, X.; Hao, H. Multiple stimuli-responsive flexible crystal with 2D elastic bending, plastic twisting and photoinduced bending capabilities. *J. Mater. Chem. C* **2021**, *9*, 16762–16770.

(28) Koshima, H.; Uchimoto, H.; Taniguchi, T.; Nakamura, J.; Asahi, T.; Asahi, T. Mechanical motion of molecular crystals induced by [4 + 4] photodimerisation. *CrystEngComm* **2016**, *18*, 7305–7310.

(29) Zhu, L.; Al-Kaysi, R. O.; Dillon, R. J.; Tham, F. S.; Bardeen, C. J. Crystal Structures and Photophysical Properties of 9-Anthracene Carboxylic Acid Derivatives for Photomechanical Applications. *Cryst. Growth Des.* **2011**, *11*, 4975–4983.

(30) Zhu, L.; Tong, F.; Salinas, C.; Al-Muhanna, M. K.; Tham, F. S.; Kisailus, D.; Al-Kaysi, R. O.; Bardeen, C. J. Improved Solid-State Photomechanical Materials by Fluorine Substitution of 9-Anthracene Carboxylic Acid. *Chem. Mater.* **2014**, *26*, 6007–6015.

(31) Gately, T. J.; Sontising, W.; Easley, C. J.; Islam, I.; Al-Kaysi, R. O.; Beran, G. J. O.; Bardeen, C. J. Effect of halogen substitution on energies and dynamics of reversible photomechanical crystals based on 9-anthracenecarboxylic acid. *CrystEngComm* **2021**, *23*, 5931–5943.

(32) Al-Kaysi, R. O.; Bardeen, C. J. Reversible photoinduced shape changes of crystalline organic nanorods. *Adv. Mater.* **2007**, *19*, 1276–1280.

(33) Zhu, L.; Al-Kaysi, R. O.; Bardeen, C. J. Reversible Photoinduced Twisting of Molecular Crystal Microribbons. *J. Am. Chem. Soc.* **2011**, *133*, 12569–12575.

(34) Yang, C.; Zhu, L.; Kudla, R. A.; Hartman, J. D.; Al-Kaysi, R. O.; Monaco, S.; Schatschneider, B.; Magalhaes, A.; Beran, G. J. O.; Bardeen, C. J.; Mueller, L. J. Crystal structure of the meta-stable intermediate in the photomechanical, crystal-to-crystal reaction of 9-tertbutyl anthracene ester. *CrystEngComm* **2016**, *18*, 7319–7329.

(35) Chalek, K. R. et al. Bridging photochemistry and photomechanics with NMR crystallography: the molecular basis for the macroscopic expansion of an anthracene ester nanorod. *Chem. Sci.* **2021**, *12*, 453–463.

(36) Beran, G. J. O. First-principles computations indicate that solid state photodimerization of 9-*tert*-butyl anthracene ester produces an exceptionally metastable polymorph. *CrystEngComm* **2019**, *21*, 758–764.

(37) Gately, T. J.; Cook, C. C.; Almuzarie, R.; Islam, I.; Gardner, Z. T.; Iuliucci, R. J.; Al-Kaysi, R. O.; Beran, G. J. O.; Bardeen, C. J. Effect of fluorination on polymorphism and the photomechanical performance of cinnamalmalonitrile crystals. *Cryst. Growth Des.* **2022**, *22*, 7298–7307.

(38) Cook, C. J.; Li, W.; Lui, B. F.; Gately, T. J.; Al-Kaysi, R. O.; Mueller, L. J.; Bardeen, C. J.; Beran, G. J. O. A theoretical framework for the design of photomechanical engines. *Chem. Sci.* **2022**, *14*, 937–949.

(39) Cook, C. J.; Perry, C. J.; Beran, G. J. O. Organic crystal packing is key to determining the photomechanical response. *J. Phys. Chem. Lett.* **2023**, *14*, 6823–6831.

(40) Moré, R.; Busse, G.; Hallmann, J.; Paulmann, C.; Scholz, M.; Techert, S. Photodimerization of Crystalline 9-Anthracenecarboxylic Acid: A Nontopotactic Autocatalytic Transformation. *J. Phys. Chem. C* **2010**, *114*, 4142–4148.

(41) Giannozzi, P. et al. Advanced capabilities for materials modelling with Quantum ESPRESSO. *J. Phys. Condens. Mat.* **2017**, *29*, 465901.

(42) Becke, A. D. On the large-gradient behavior of the density functional exchange energy. *J. Chem. Phys.* **1986**, *85*, 7184–7187.

(43) Perdew, J. P.; Burke, K.; Ernzerhof, M. Generalized gradient approximation made simple. *Phys. Rev. Lett.* **1996**, *77*, 3865.

(44) Otero-de-la Roza, A.; Johnson, E. R. Van der Waals interactions in solids using the exchange-hole dipole moment model. *J. Chem. Phys.* **2012**, *136*, 174109.

(45) Cohen, A. J.; Mori-Sánchez, P.; Yang, W. Challenges for Density Functional Theory. *Chem. Rev.* **2012**, *112*, 289–320.

(46) Bryenton, K. R.; Adeleke, A. A.; Dale, S. G.; Johnson, E. R. Delocalization error: The greatest outstanding challenge in density-functional theory. *WIREs Comput. Mol. Sci.* **2022**, 29–32.

(47) Grimme, S.; Diedrich, C.; Korth, M. The Importance of Inter- and Intramolecular van der Waals Interactions in Organic Reactions: the Dimerization of Anthracene Revisited. *Angew. Chem. Int. Ed.* **2006**, *45*, 625–629.

(48) Greenwell, C.; Řezáč, J.; Beran, G. J. O. Spin-component-scaled and dispersion-corrected second-order Møller-Plesset perturbation theory: An alternative path toward chemical accuracy. *Phys. Chem. Chem. Phys.* **2022**, *24*, 3695–3712.

(49) Greenwell, C.; Beran, G. J. O. Inaccurate conformational energies still hinder crystal structure prediction in flexible organic molecules. *Cryst. Growth Des.* **2020**, *20*, 4875–4881.

(50) Smith, D. G. A. et al. PSI4 1.4: Open-source software for high-throughput quantum chemistry. *J. Chem. Phys.* **2020**, *152*, 184108.

(51) The MP2D software can be downloaded at `https://github.com/Chandemonium/MP2D`.

(52) Helgaker, T.; Klopper, W.; Koch, H.; Noga, J. Basis-set convergence of correlated calculations on water. *J. Chem. Phys.* **1997**, *106*, 9639–9646.

(53) Dunning, T. H. Gaussian basis sets for use in correlated molecular calculations. I. The atoms boron through neon and hydrogen. *J. Chem. Phys.* **1989**, *90*, 1007–1023.

(54) Rai, S. K.; Gunnam, A.; Beran, G. J. O.; Kaduk, J. A.; Nangia, A. K. Polymorphs, solvatomorphs, hydrate, and perhydrate of dabrafenib. *Cryst. Growth Des.* **2023**, *23*, 1179–1188.

(55) Greenwell, C.; Beran, G. J. O. Rubrene untwisted: common density functional theory calculations overestimate its deviant tendencies. *J. Mater. Chem. C* **2021**, *9*, 2848–2857.

(56) Beran, G. J. O.; Sugden, I. J.; Greenwell, C.; Bowskill, D. H.; Pantelides, C. C.; Adjiman, C. S. How many more polymorphs of ROY remain undiscovered? *Chem. Sci.* **2022**, *13*, 1288–1297.

(57) Beran, G. J. O.; Wright, S. E.; Greenwell, C.; Cruz-Cabeza, A. J. The interplay of intra- and intermolecular errors in modeling conformational polymorphs. *J. Chem. Phys.* **2022**, *156*, 104112.

(58) Chisholm, J. A.; Motherwell, W. D. S. COMPACK: A program for identifying crystal structure similarity using distances. *J. Appl. Crystall.* **2005**, *38*, 228–231.

For Table of Contents Use Only

Title: "Understanding the impact of halogenation on the crystalline photomechanical response properties of 9-anthracene carboxylic acid from first-principles"

Authors: Cody J. Perry and Gregory J. O. Beran

TOC graphic:

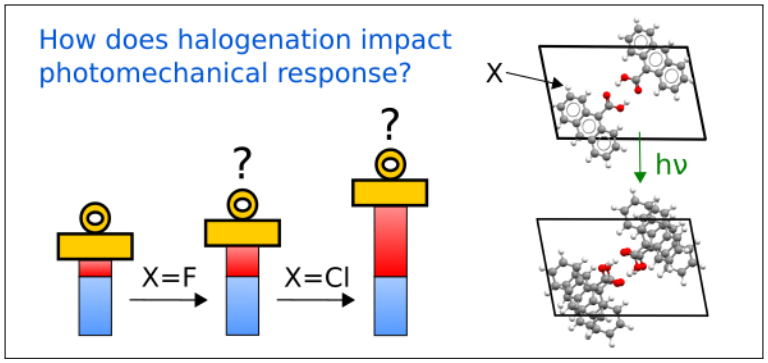

Synopsis: To elucidate relationships between molecular structure and solid-state photomechanical response, density functional theory calculations are used to investigate how halogen substitution alters the crystal structure transformations and photomechanical work densities produced by the solid-state photodimerization of 9-anthracene carboxylic acid.